

A Kinetic Study of the Intercalation of Lithium Salts into $\text{Al}(\text{OH})_3$

Gareth R. Williams and Dermot O'Hare*

Chemistry Research Laboratory, Department of Chemistry, University of Oxford, Mansfield Road, Oxford OX1 3TA, U.K.

Received: December 7, 2005; In Final Form: April 4, 2006

The intercalation of five lithium salts into the gibbsite and bayerite polymorphs of $\text{Al}(\text{OH})_3$ has been studied using in situ energy-dispersive X-ray diffraction. The kinetics and mechanisms of the reactions have been modeled using the Avrami–Erofe'ev model. The kinetic data suggest that the reaction mechanisms are predominantly nucleation controlled, although the intercalation of LiNO_3 into bayerite and of Li_2SO_4 into gibbsite proceed via two-stage mechanisms, one part of which is diffusion controlled. All the reactions proceed directly from the host to the product, except for the intercalation of Li_2SO_4 into gibbsite where a more hydrated intermediate form of $[\text{LiAl}_2(\text{OH})_6]_2\text{SO}_4 \cdot y\text{H}_2\text{O}$ is generated prior to the final product.

Introduction

The family of layered double hydroxides (LDHs) $[\text{LiAl}_2(\text{OH})_6]\text{X}_y \cdot y\text{H}_2\text{O}$ ($\text{LiAl}_2\text{--X}$) is the only set of LDHs to contain +1 and +3 cations. The first of these compounds to be synthesized was $[\text{LiAl}_2(\text{OH})_6](\text{CO}_3)_{0.5} \cdot y\text{H}_2\text{O}$, which was produced via the hydrolysis of aluminum tris(*sec*-butoxide) in the presence of Li_2CO_3 .¹ There exists, however, a more general preparative route allowing the synthesis of materials with a variety of interlayer anions X (for example, X = Cl, Br, I, HO, NO_3 , CO_3 , SO_4 , and CH_3CO_2). This involves the direct reaction of gibbsite or bayerite (polymorphs of $\text{Al}(\text{OH})_3$) with concentrated solutions of Li salts.^{2–4} Alternative methods include a hydrothermal preparation of $\text{LiAl}_2\text{--OH}$ from hydrated alumina gel and LiOH .⁵

It has recently been demonstrated that the LiX intercalates of gibbsite crystallize in hexagonal symmetry with an *aba* layer stacking sequence,⁶ but the bayerite intercalates have rhombohedral symmetry with an *abca* sequence.⁷ The use of different polymorphs of $\text{Al}(\text{OH})_3$ as starting materials results in related LDHs that differ in the stacking sequence of the layers. The hexagonal materials will henceforth be denoted h- $\text{LiAl}_2\text{--X}$ and the rhombohedral analogues as r- $\text{LiAl}_2\text{--X}$.

The stabilities of the h- $\text{LiAl}_2\text{--X}$ materials upon heating in water have been studied previously.^{8–12} Treatment below 150 °C results in deintercalation of the lithium salts and the production of $\text{Al}(\text{OH})_3$, whereas reaction above 150 °C produces boehmite (AlOOH) in addition to the solvated salts. The intercalation and deintercalation of LiX is reversible in this system. No Al^{3+} cations were observed in the supernatant solution, confirming that there is no dissolution of the hydroxide matrix during the process: the reaction is perfectly topochemical. Treatment of the recovered $\text{Al}(\text{OH})_3$ with LiX results in the re-formation of the $\text{LiAl}_2\text{--X}$ materials.

Recent findings have shown that the intercalation–deintercalation cycle has a profound effect on the polydispersity and morphology of the $\text{Al}(\text{OH})_3$ particles,^{11,12} leading to significant increases in the specific surface area (by a factor of 30–50). In addition, there is commonly a trace sodium content in $\text{Al}(\text{OH})_3$,

which arises from the use of concentrated NaOH solutions in the production method. The Na content is significantly reduced after the LiX intercalation–deintercalation cycle,^{13,14} which is beneficial for the production of Na-free $\text{Al}(\text{OH})_3$ or Al_2O_3 -based catalysts and solid supports.

Although these processes have received a significant amount of attention in recent years, there is a distinct lack of quantitative information on the intercalation and deintercalation processes. This is significant for fundamental reasons, since the reactions are highly unusual in that both anions and cations are simultaneously incorporated into the host lattice. In addition, the production of Na-free Al oxides and hydroxides is of industrial interest for a number of catalytic applications. Furthermore, the LDHs which result from the reactions have the potential to be used in a number of processes, including the separation of isomeric pairs.^{15–17} An understanding of their formation, and how the precise nature of the products might be controlled, is of great importance. Recent work by O'Hare and co-workers^{18,19} has begun to address this deficiency, but the picture is still far from complete. The intercalation and deintercalation cycle involving LiCl and gibbsite has been comprehensively explored, but only a very limited amount of data regarding the reactions of other salts have been obtained.¹⁸ In addition, no experiments have been performed to investigate the analogous reactions with bayerite. Since it is known that the reaction products of the gibbsite and bayerite starting materials are different, it was of interest to see if the different polymorphic $\text{Al}(\text{OH})_3$ hosts have different intercalation mechanisms and kinetics. Therefore, the work described in this contribution is an extension of previous studies. An extensive systematic investigation into the intercalation of a wide variety of LiX salts is reported.

Experimental Section

Starting Materials. Gibbsite was supplied by Alcoa or Aughinish Alumina and was used as supplied. Bayerite was synthesized using the method of Thomas and Sherwood.²⁰ Activated gibbsite was prepared by grinding for 7 days in a Pascall Engineering 9VS ball mill operating at ca. 50% speed. Lithium salts were supplied by Aldrich or Lancaster ($\geq 98\%$) and were used as supplied.

Time-Resolved in-Situ Energy-Dispersive X-ray Diffraction (EDXRD) Experiments. Experiments were carried out on

* Corresponding author. Tel: +44 1865 285130. Fax: +44 1865 285131. E-mail: dermot.ohare@chem.ox.ac.uk.

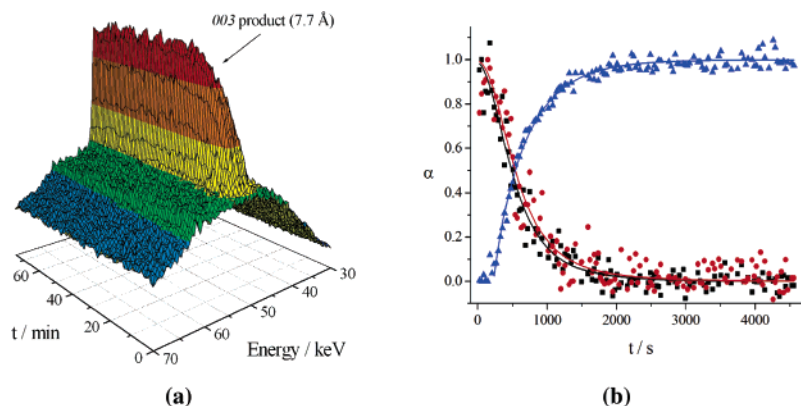


Figure 1. In situ EDXRD data showing the course of the reaction between bayerite and 10 M LiCl at 130 °C: (a) 3D stacked plot showing the gain in intensity of the LDH 003 reflection with time; (b) plot of extent of reaction vs time, showing the bayerite 001 (black squares) and 110 (red circles) and the r-LiAl₂-Cl 003 (blue triangles) reflections. The bayerite reflections occur outside the energy range visible in (a) and, hence, cannot be seen.

Station 16.4 of the U.K. Synchrotron Radiation Source (SRS) at the Daresbury Laboratory. Intercalation reactions were performed in glass ampoules contained within a temperature-controlled block, the details of which have been discussed previously.^{21–23} A 0.5 g amount of the desired Al(OH)₃ polymorph was placed into an ampule with a magnetic stirrer bar. A 10 mL volume of the appropriate Li salt solution was added and the ampule sealed using a rubber septum. This was heated to the reaction temperature, and EDXRD patterns were recorded with an acquisition time of 30 s. Values of 2θ between 1.3 and 2.2° were used, depending on the basal spacing of the anticipated product. Data were recorded until the intensity of the product Bragg reflections stopped increasing. The solid products were isolated, washed, dried, and characterized using X-ray powder diffraction (XRD), elemental analysis (EA), and IR spectroscopy.

Data Analysis. An automated Gaussian fitting routine is used to obtain the peak areas of the Bragg reflections.²⁴ These values are subsequently converted to the extent of reaction at time *t*, α(*t*), defined as α(*t*) = *I*_{hkl}(*t*)/*I*_{hkl}(max), where *I*_{hkl}(*t*) is the area of a given peak at time *t* and *I*_{hkl}(max) is the maximum area of this peak. The intercalation processes were modeled using the Avrami–Erofe’ev model. This is the most commonly employed approach for describing solid-state reaction processes. This rate law has been derived in a number of ways, indicating its general applicability and validity. The equation takes the form

$$[-\ln(1 - \alpha)]^{1/n} = k(t - t_{\text{ind}}) \quad (1)$$

where *t*_{ind} is the induction time for the reaction. This expression has been successfully applied to a number of solid-state processes, including phase transformations,²⁵ decompositions,²⁶ crystallization, and intercalation reactions.^{27,28} The equation is found to fit most closely with the experimental data within the range 0.15 < α < 0.85.^{29,30}

The Avrami model was originally devised for homogeneous systems; therefore, adaptations in the interpretation of this are required when considering intercalation processes. In particular, it is generally accepted that the nucleation sites are the edges of the layers, where the guest species in solution can gain access to the interlayer region. This means that either deceleratory or instantaneous nucleation is possible: constant nucleation is not an option, since all the potential nucleation sites exist at the start of the reaction. This will be discussed in more detail in the text below and is the subject of a recent review.³¹ At this point, it should be noted that the Avrami model is a simplifica-

tion of the actual nanoscopic processes occurring during an intercalation reaction. A number of variants of the Avrami model exist; however, the intercalation reactions studied are enormously complex processes. To make comparisons between different data sets possible and to avoid assigning effects to factors arbitrarily, it is generally considered that the Avrami model is the best to use at this juncture in time until more is understood about the processes involved.

The most facile way to check the validity of the Avrami model is to generate a Sharp–Hancock plot of (ln(−ln(1 − α))) vs ln *t*.²⁶ A linear Sharp–Hancock plot is indicative of the Avrami model being applicable.

Characterization. *Powder X-ray Diffraction.* Powder XRD patterns were recorded on a PANalytical X’Pert Pro diffractometer at 40 kV and 40 mA, using Cu Kα radiation.

Infrared Spectroscopy. Infrared experiments were carried out using a Perkin-Elmer 1600 series FTIR spectrometer. Samples were mixed with KBr and made into pellets, and spectra were recorded between 4000 and 400 cm^{−1}. A total of 32 scans were recorded with a scan resolution of 4 cm^{−1}.

Results

Intercalation of LiCl into Bayerite. Temperature Dependence. The temperature dependence of this reaction was investigated over the range 70–140 °C. In all cases, the reaction was observed to proceed directly from bayerite to the r-LiAl₂-Cl LDH: no intermediates could be seen. The time evolution of the reaction of bayerite with 10 M LiCl at 130 °C is shown in Figure 1.

The one-step nature of the intercalation process is clear from the data in Figure 1b. The α vs time curves of the host and product reflections are observed to cross close to α = 0.5. This means that as coherence from the host material is lost, there is a matching gain in coherence from the product phase. This is consistent only with a process in which the host is transformed directly into the product: if there were intermediates formed, then the loss in intensity from the host material would be more rapid than the gain in intensity from the product. The solids isolated at the end of each reaction were analyzed ex situ and were found to have the formula [LiAl₂(OH)₆]Cl·*y*H₂O (*y* = 1–2). The ex situ X-ray powder diffraction (XRD) patterns of the products closely resembled that reported by Fogg et al. for the r-LiAl₂-Cl LDH.⁷

In each case, the Avrami–Erofe’ev model was fitted to the experimental data (Figure 2a). Sharp–Hancock plots were

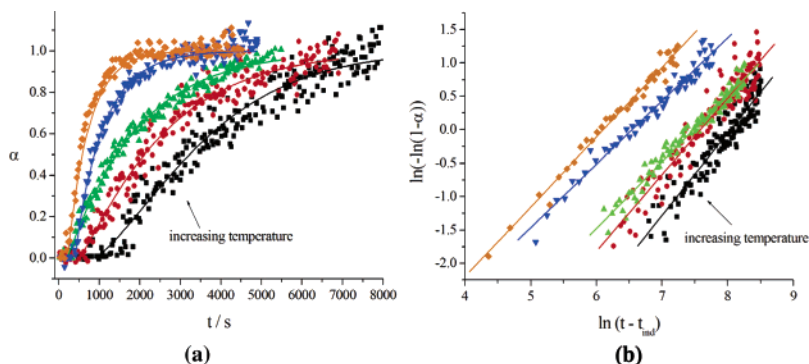


Figure 2. (a) Extent of reaction plotted against time for the intercalation of LiCl (10 M) into bayerite at 80 °C (black squares), 90 °C (red circles), 100 °C (green triangles), 120 °C (blue triangles), and 130 °C (orange diamonds). Data at 140 °C have been omitted for clarity. The data have been fitted with the Avrami–Erofe’ev equation with $n = 1$. (b) Sharp–Hancock plots of $\ln(-\ln(1 - \alpha))$ vs $\ln t$ at the same temperatures. The linear nature of the plots confirms the validity of the Avrami–Erofe’ev model for this process.

TABLE 1: Kinetic Parameters for the Intercalation of LiCl into Bayerite as a Function of Temperature

$T/^\circ\text{C}$	n	$k/10^{-3} \text{ s}^{-1}$	$t_{0.5}/\text{s}$	t_{ind}/s
80	1.22 ± 0.04	0.32 ± 0.02	3250	840
90	1.14 ± 0.03	0.45 ± 0.03	2100	520
100	1.00 ± 0.02	0.57 ± 0.03	1350	410
120	0.95 ± 0.02	1.13 ± 0.07	900	270
130	1.04 ± 0.02	1.38 ± 0.07	680	220
140	0.84 ± 0.02	1.90 ± 0.17	510	210

generated to calculate the value of the reaction exponent, n (Figure 2b). The rate constants, k , were then determined by fixing the exponent n to its idealized value and fitting the Avrami expression to the experimental curves. These kinetic data are summarized in Table 1. As is intuitively anticipated, the rate of reaction was observed to increase with temperature. There is a significant induction time at lower temperatures: in contrast, no induction time is seen for the analogous reactions with gibbsite.¹⁸ The rates of reaction are generally comparable with those for the gibbsite reactions, being slightly higher at the majority of temperatures. There is a greater amount of scatter in the data collected at lower temperatures. This is due to the lower crystallinity of the LDH formed at lower temperatures with respect to samples generated at elevated temperatures. This leads to broader Bragg reflections, which are harder to resolve using the energy dispersive detector.

The value of n is found to be approximately 1 at all temperatures: indeed, fixing $n = 1$ produces good fits to the experimental data in all cases (see Figure 2a). This is consistent with a nucleation-growth mechanism which is two-dimensional diffusion controlled following instantaneous nucleation. Instantaneous nucleation refers to a situation in which all the potential nucleation sites (i.e. the edges of the layers) are saturated at the start of the reaction. The rate-limiting step is then likely to be expansion of the interlayer spaces to accommodate the first guest species to intercalate. Once a pair of layers have been prised apart, the guests are free to diffuse into the interlayer region (hence 2D diffusion). Once the Li–Cl ion pair is accommodated between the layers, it is likely that it will be facile for the Li^+ cations to move up into the voids in the layers. Plots of α vs reduced time $((t - t_{\text{ind}})/t_{0.5})$ have been shown to be superimposable within experimental error (this plot is included in the Supporting Information), confirming that the reaction proceeds via the same mechanism at all the temperatures studied. The temperature dependence of the reaction rate has been used to calculate the activation energy for the process via the Arrhenius equation, $k = Ae^{-E_a/RT}$. A plot of $\ln k$ vs $1/T$ is given in Figure 3. A value of $43.0 \pm 1.2 \text{ kJ mol}^{-1}$ is calculated

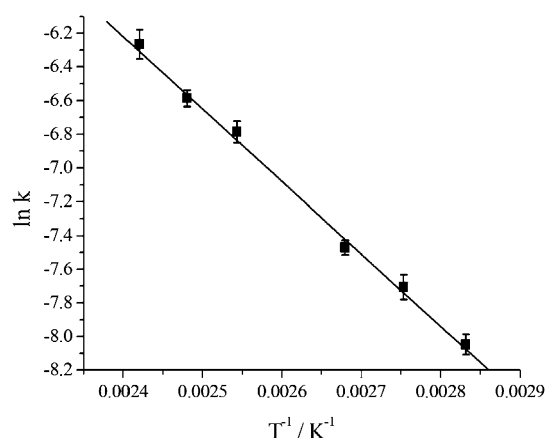


Figure 3. Arrhenius plot to determine the activation energy for the intercalation of LiCl into bayerite.

TABLE 2: Kinetic Parameters for the Intercalation of LiCl into Bayerite as a Function of LiCl Concentration

$[\text{LiCl}]/\text{M}$	n	$k/10^{-3} \text{ s}^{-1}$	$t_{0.5}/\text{s}$	t_{ind}/s
4	1.31 ± 0.03			1800
5	1.28 ± 0.02	0.60 ± 0.03	2860	510
7.5	1.07 ± 0.02	0.86 ± 0.05	1270	410
10	0.95 ± 0.02	1.13 ± 0.07	720	270
12	1.02 ± 0.03	1.84 ± 0.12	450	210
15	0.96 ± 0.03	3.86 ± 0.30	240	60

for the activation energy. This is 16 kJ mol^{-1} higher than the activation energy for gibbsite intercalation.

Concentration Dependence. A second series of experiments was performed at 120 °C to elucidate the effect of varying the LiCl concentration over the range 4–15 M. The experimental data are given in the Supporting Information (Figure S2). Values of n and k were calculated in the same way as described above: the parameters are summarized in Table 2. The rate of reaction is observed to be very sensitive to the concentration of LiCl, as was the case for the analogous gibbsite reactions. Reactions using 4 M LiCl did not reach completion even after 3 h. Plots of α vs reduced time were found to be superimposable, confirming that the same mechanism is operational in each case. The exponent n is close to one in all cases, implying a 2D diffusion-controlled mechanism following instantaneous nucleation. However, n increases as the concentration of LiCl is decreased, suggesting that nucleation becomes more important as the concentration falls. This relates to the rate of transport of the guest to the host, which will clearly be reduced at low concentrations. Hence, saturation of the nucleation sites is more difficult at low LiCl concentration, and nucleation assumes an

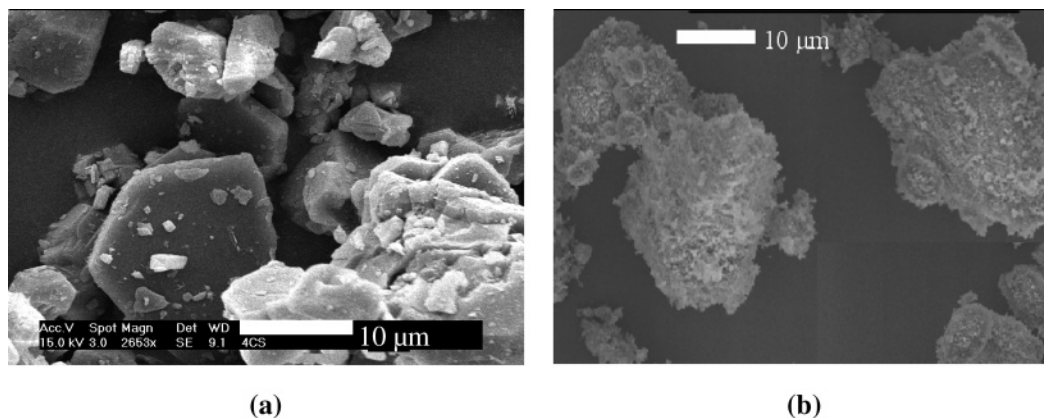


Figure 4. Scanning electron microscopy images of (a) gibbsite and (b) bayerite.

increased importance. At very low concentrations, it appears likely that deceleratory nucleation may be the dominant mechanism (this occurs when the rate of transport of the guest to the host is low).

The order of reaction with respect to [LiCl] can be determined by plotting $\ln k$ vs $\ln [\text{LiCl}]$. The relationship observed is far from linear: indeed, an exponential relationship provides the best fit to the experimental data points. At low concentrations of LiCl, the data points can be reasonably fitted with a line of gradient 1.12 ± 0.20 . This suggests that the reaction is first order with respect to [LiCl] when [LiCl] is below 10 M, giving the following rate equation:

$$\text{rate} \propto [\text{LiCl}]^1 \quad (2)$$

This is very different from the gibbsite case, where the reaction order was determined to be ca. 0.5. Therefore, the intercalation reactions of bayerite are much more sensitive to the guest concentration than those of gibbsite. It is postulated that the exponential relationship arises from there being a change in reaction mechanism over the concentration range studied, with an increase in the importance of nucleation at low concentrations.

Particle Size Study. The particle sizes of the gibbsite and bayerite materials used in this study have been determined using the Rietveld method³² and were calculated to be ca. 1.4 and 0.8 μm , respectively. Inspection of SEM images of the two forms of $\text{Al}(\text{OH})_3$ reveals differences in their particle morphologies (Figure 4). The gibbsite sample possesses more regular particle morphologies, whereas the bayerite polymorph consists of agglomerates of irregularly shaped particles. To more fully understand the effect that particle size and morphology has on the reaction mechanism and kinetics, experiments were performed using three further samples of gibbsite: coarse seed gibbsite (CSG); fine seed gibbsite (FSG); activated gibbsite (AG). The former two were obtained from Aughinish Alumina and had particle sizes of 0.9 and 1.5 μm , respectively. The latter sample was prepared by grinding the original gibbsite sample in a ball mill for 1 week; the particle size was ca. 0.3 μm . The intercalation of LiCl was then monitored over the temperature range 80–120 $^\circ\text{C}$. Extent of reaction vs time plots for the reaction of each sample at 110 $^\circ\text{C}$ are given in Figure 5. For comparison, the kinetic data for each sample collected at 110 $^\circ\text{C}$ are included in Table 3. The full data are included in the Supporting Information.

The above data reveal a strong dependence of reaction rate and mechanism on the particle size and morphology. For the CSG sample, the exponent n is close to one, and the reaction proceeds only after a significant induction time. The FSG sample

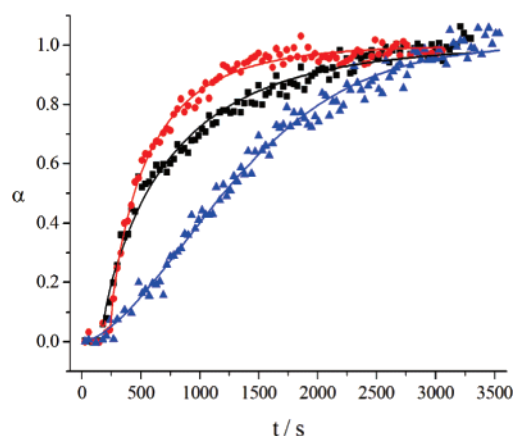


Figure 5. Extent of reaction vs time plots for the intercalation of 10 M into coarse seed gibbsite (black squares), fine seed gibbsite (red circles), and activated gibbsite (blue triangles) at 110 $^\circ\text{C}$.

TABLE 3: Kinetic Parameters for the Intercalation of 10 M Lithium Chloride into the Different Gibbsite Samples at 110 $^\circ\text{C}$

sample	n	$k/10^{-3} \text{ s}^{-1}$	$t_{0.5}/\text{s}$	t_{ind}/s
FSG	0.73 ± 0.02	2.08 ± 0.15	435	235
CSG	0.76 ± 0.02	1.49 ± 0.14	470	160
AG	1.60 ± 0.03	0.67 ± 0.05	1200	

has generally somewhat lower n values, suggesting that nucleation is less important in this case. An exponent close to one suggests 2D diffusion control following instantaneous nucleation, as recorded for previous intercalation reactions (see above). In contrast, the AG sample has $n \approx 1.5$, consistent with 2D diffusion control following deceleratory nucleation. Additionally, no induction time is seen here. It is generally observed that the value of the exponent n , and hence the importance of nucleation, falls as the particle size increases.

The activation energies are $29.3 \pm 2.2 \text{ kJ mol}^{-1}$ for CSG, $26.1 \pm 4.3 \text{ kJ mol}^{-1}$ for FSG, and $49.7 \pm 8.8 \text{ kJ mol}^{-1}$ for AG. These may be compared with the value of 27 kJ mol^{-1} for the normal gibbsite sample.¹⁸ It appears, therefore, that the importance of nucleation increases with decreasing particle size, and E_a increases concomitantly. This is not completely intuitive but may be understood by recognizing that the amount of gibbsite present in each case is the same. The rate-determining step of the reaction is the expansion of the interlayer space to accommodate the guests: once a pair of layers has been prised apart, it is facile for the guests to fill the interlayer space. Therefore, in a sample with smaller particle sizes, more nucleation events are required for the reaction to reach completion, owing to the sample consisting of a greater number of smaller particles. E_a

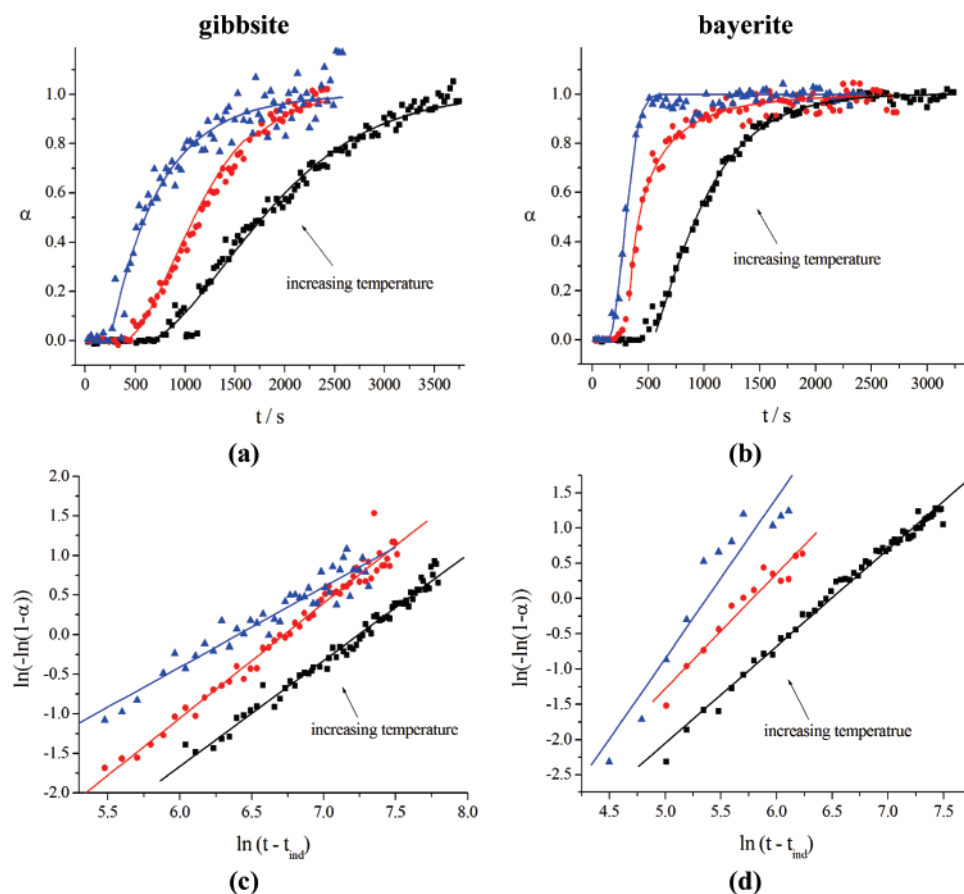


Figure 6. EDRXD data for the intercalation of LiOH into $\text{Al}(\text{OH})_3$ at 70 °C (black squares), 90 °C (red circles), and 110 °C (blue triangles). The data points shown illustrate the growth of the 002 reflection of $\text{h-LiAl}_2\text{-OH}$ or the 003 reflection of $\text{r-LiAl}_2\text{-OH}$. Data at 80, 100, and 120 °C have been omitted for clarity. In (a) and (b), least-squares fits of the Avrami–Erofe’ev equation to the data for (a) gibbsite and (b) bayerite are shown. In (c) and (d), Sharp–Hancock plots for (c) gibbsite and (d) bayerite are given.

for the process is thus increased. For the normal, CSG, and FSG samples, the nucleation sites are all saturated at the start of the reaction: in contrast, deceleratory nucleation is seen for the AG sample owing to the much greater number of possible nucleation sites present.

Isupov et al. have performed microscopy experiments investigating the nature of the particulates before and after reaction and also the distribution of Li and Cl in partially reacted systems.³³ Their proposed mechanism involves the Li cations, the anions, and water molecules attacking the surface of the solid, penetrating between the layers from the layer edges to the center of the particles. In the first stage of the reaction, the Li^+ cations are believed to be incorporated into the interlayer space. In order for this to happen, the Li^+ ions must shed their aqueous shell. Once positioned between the layers, electrostatic repulsion between the Li^+ ions and the gibbsite protons (which link the layers through H-bonding) will force the layers further apart. Once the H-bonds are weakened, the intercalation of additional cations and anions is facilitated.

Subsequently, as the Li cations move from the interlayer space into the vacancies in the $\text{Al}(\text{OH})_3$ layers, some reorganization of the OH groups in the layers occurs. The interlayer distance is drastically increased by intercalation, and thus elastic strains arise at the gibbsite–intercalate interfaces. These relax either by dispersion of the starting gibbsite or by its plastic deformation. Hence, packing defects are introduced, and the initial spherical-like particles of gibbsite are turned into platelike LDH particles. The data for the intercalation of LiCl into both gibbsite and bayerite concur with this mechanism. The rate-determining step is seen to be the expansion of the interlayer space to

accommodate the guest ions. Once this has occurred, it is relatively easy for other ions and water molecules to fill this space.

The difference in concentration dependence between bayerite and gibbsite (the reaction is half-order with respect to LiCl concentration for gibbsite but first-order in the bayerite case) is less intuitive but may also be linked to the greater number of packing faults in the bayerite system. Additional packing defects and reduced particle regularity will result in the availability of a greater number of nucleation sites, which it is more difficult to saturate. This concurs with the results from the intercalation of LiCl into different gibbsite samples, where it was observed that larger particles sizes led to shorter induction times and a reduced importance of nucleation.

Intercalation of LiOH . The intercalation of LiOH into both gibbsite and bayerite was monitored as a function of temperature and concentration. The intercalation of LiOH into both polymorphs of $\text{Al}(\text{OH})_3$ demonstrated a profound temperature dependence, with the reaction rate increasing rapidly with temperature. As was the case for the intercalation of LiCl into bayerite, an induction time was observed before the reaction began. A 5 M solution of LiOH was used for each experiment. Least-squares fits of the Avrami equation to the experimental data for gibbsite and bayerite are depicted in Figure 6a,b respectively: the Sharp–Hancock plots used to determine n are illustrated in Figure 6c,d. The kinetic parameters for the gibbsite and bayerite reactions are summarized in the Supporting Information (Tables S1 and S2). It can be seen that the rate constants for gibbsite are significantly lower than those for bayerite. This is additionally visible from the plots in Figure

6a,b: not only is the induction time noticeably longer in the gibbsite case, but once the reaction starts, it proceeds much more slowly. In both cases, there is significant variation in the values of the exponents, making mechanistic deductions difficult. For this reason, k was determined directly from Sharp–Hancock plots. In the majority of cases, for both polymorphic starting materials, n lies between 1 and 2. This is consistent with a mechanism which is 2D diffusion controlled following deceleratory nucleation. This suggests that the nucleation sites are activated one-by-one, rather than being saturated at the start of the reaction. This may be attributed to the higher solvation energy of the HO^- ion (cf. Cl^-).

The activation energies have been calculated from the Arrhenius equation: for gibbsite, $E_a = 22.0 \pm 2.0 \text{ kJ mol}^{-1}$, and for bayerite $E_a = 20.9 \pm 4.8 \text{ kJ mol}^{-1}$. The small difference in E_a (in fact, the two values are identical within experimental error) is surprising, since the rate constant for intercalation into bayerite is generally approximately twice that for gibbsite. However, the large error in the bayerite E_a value means that this should be treated with caution. In both cases, the E_a is lower than for LiCl intercalation.

Experiments were performed to investigate the concentration dependence of the intercalation of LiOH into both polymorphs of LiOH. The crystallinity of the bayerite intercalates was found to be significantly lower than that of the gibbsite analogues. This led to problems monitoring the reaction at low LiOH concentrations, because it was unclear when the reaction was complete. Therefore, no accurate parameters could be obtained for the bayerite intercalation processes. The values of n obtained for the gibbsite reaction suggest the mechanism is 2D diffusion controlled following deceleratory nucleation. The induction time and half-life decrease rapidly with increasing concentration. The order of reaction with respect to $[\text{LiOH}]$ was determined to be 0.84 ± 0.04 .

Intercalation of LiNO_3 . Intercalation into Gibbsite. The intercalation of LiNO_3 into gibbsite was observed to be highly capricious. Fogg et al. found that the intercalation of 5 M LiNO_3 was extremely slow at 120°C , failing to reach completion in 6 h. Therefore, attempts were made to monitor this process using more concentrated solutions. In the majority of cases, the reactions were found to proceed too rapidly for the collection of sufficient data to deduce either kinetic or mechanistic information, even at temperatures as low as 60°C .

However, some information could still be obtained. The reactions are observed to proceed directly from the host to the product phase in all cases, with no intermediates forming. There is additionally an induction time, which varies with temperature, before the reaction begins. A sample data set is provided in Figure 7.

The induction period is clearly visible here. Following this, there is very rapid conversion of the host to the product, which makes calculation of n and k difficult. n was observed to lie in the region of 1–2 for all the reactions monitored. This corresponds to a mechanism which is 2D diffusion controlled after deceleratory nucleation. The α vs time curves of the host and product materials are observed to cross at $\alpha \approx 0.5$, which confirms the one-step nature of the reaction.

Intercalation into Bayerite. The intercalation of LiNO_3 into bayerite also proceeded directly from the host to the product. The reaction proved to be very slow, in contrast to the gibbsite case, and it was necessary to use a 15 M solution of lithium nitrate with elevated temperatures to drive the reaction to completion. The shapes of the α vs time curves were curious (Figure 8a), and the Avrami equation provided only a relatively

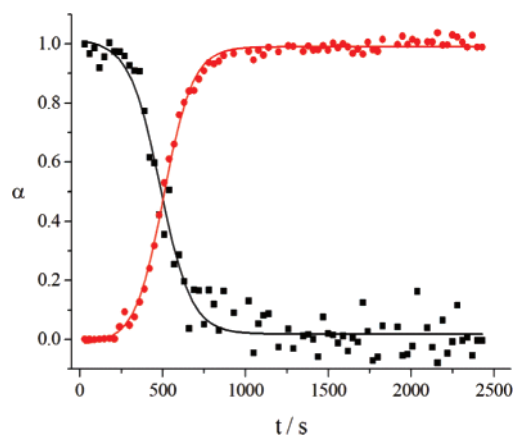


Figure 7. Extent of reaction vs time plot for the intercalation of 6 M LiNO_3 into gibbsite at 60°C . The gibbsite 001 (black squares) and the $\text{h-LiAl}_2\text{-NO}_3$ 002 (red circles) reflections are shown.

poor fit to the experimental data. Sharp–Hancock plots revealed an abrupt change in gradient at $\alpha \approx 0.5$: this suggests that the mechanism for the early stages of the reaction is different from that at the later stages (Figure 8b). Values for the Avrami exponent n have been calculated from the Sharp–Hancock plots, both for the early and late stages of the reaction. These data are summarized in the Supporting Information (Table S3). k has been estimated from fitting the Avrami equation to the experimental data.

For the early stages of the reaction, n is ca. 0.5, corresponding to a mechanism which is entirely diffusion controlled, and nucleation plays no part in determining the reaction rate. After the mechanistic shift, the reaction becomes nucleation controlled: the values of n suggest that 2D diffusion control follows either instantaneous ($n \approx 1$) or deceleratory ($n = 1\text{--}2$) nucleation. This may be due to defects in the bayerite lattice. In the early stages of the reaction, intercalation will occur at reactive defect sites, and the E_a will be low. Thus, as soon as a guest ion reaches a defect site, it will intercalate. After a given time, the defect sites will have been consumed, and the remaining sites for reaction will be less reactive. This leads to a high-energy nucleation controlled process being adopted in the latter stages of the reaction. This is illustrated schematically in Figure 9. The activation energy is estimated to be $66.3 \pm 7.2 \text{ kJ mol}^{-1}$, consistent with the latter part of the process. It is postulated that complete nucleation control is observed in the gibbsite case owing to the reduced number of stacking sequence defects and the more regular particle morphology of this material.

Intercalation of Li_2SO_4 into Gibbsite. Temperature Studies. $T \leq 120^\circ\text{C}$. The intercalation of 3 M Li_2SO_4 into gibbsite at 100°C is illustrated in Figure 10. Contrary to the intercalation of LiOH and LiNO_3 , there is no induction time for this process. The reaction begins as soon as the Li sulfate solution is added to the host. The reaction is found to be initially very rapid, until ca. 60% of the gibbsite has reacted. Following this, there is a sustained, slower, conversion of the remaining 40% of the starting material into the product. The fitting of the Avrami equation to the data is observed to be rather poor, particularly at the point where the slope of the curve changes, at $\alpha \approx 0.6$.

The reasons behind the strange shapes of the curves and the poor fitting of the Avrami equation can be elucidated from the Sharp–Hancock plots in Figure 11. A marked discontinuity is present at approximately the midpoint in the reaction. This suggests that the reaction mechanism is not consistent over the whole course of the reaction: there is a mechanistic change

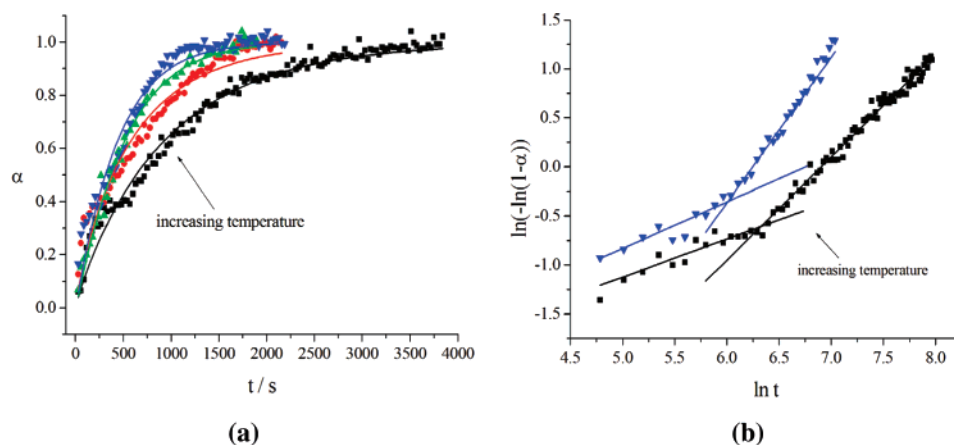


Figure 8. (a) Extent of reaction vs time plotted for the intercalation of LiNO_3 into bayerite at 125 (black squares), 130 (red circles), 135 (green triangles), and 140 °C (blue triangles). The data points are for the growth of the 003 reflection of $r\text{-LiAl}_2\text{-NO}_3$. The experimental data have been fitted with the Avrami–Erofev equation. (b) Sharp–Hancock plots at 125 (black squares) and 140 °C (blue triangles).

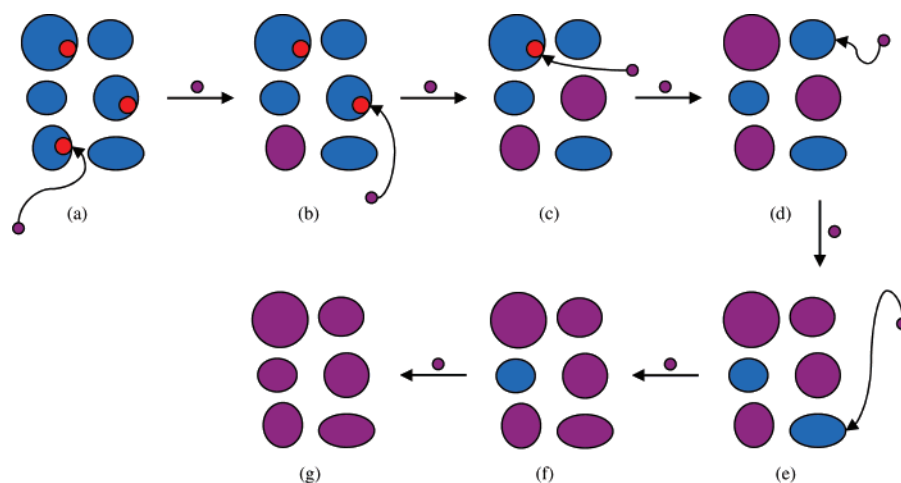


Figure 9. Schematic illustrating the two-stage intercalation process operational for the reaction of LiNO_3 with bayerite. Unreacted bayerite particles are in blue, defect sites are represented as red circles, guests are as small purple circles, and reacted bayerite particles are also colored purple. (a) The bayerite particles are shown prior to reaction, showing defect sites on three of the six particles. The first reaction is observed to occur at one of the defect sites. In (b) and (c) reaction at the remaining defect sites is shown. This is the diffusion-controlled segment of the reaction. In (d), all the defect sites have been consumed, and hence, reaction must occur at nondefect layer edges. This nucleation controlled part of the reaction continues to occur in (e) and (f) until finally the reaction is complete in (g).

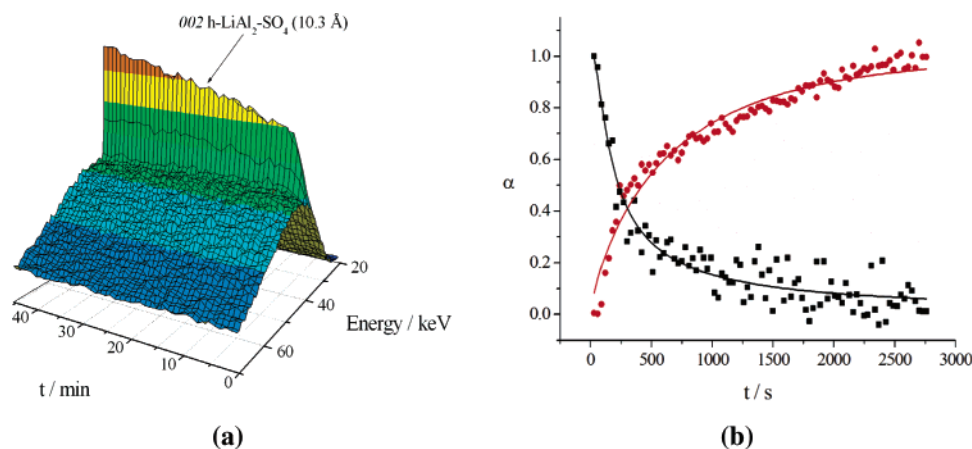


Figure 10. In situ data for the intercalation of Li_2SO_4 into gibbsite at 100 °C: (a) 3D stacked plot showing the evolution of the product 002 reflection with time; (b) extent of reaction vs time plot showing the 001 reflection of gibbsite (black squares) and the 002 reflection of the $h\text{-LiAl}_2\text{-SO}_4$ product (red circles).

beyond $\alpha \approx 0.6$. Values of n for both the low- and high- α mechanisms have been calculated and are listed in the Supporting Information (Table S3). Also provided are estimates for the overall rate constant. These have been calculated by fitting the Avrami expression to the experimental data. Care must be

taken in drawing conclusions regarding the reaction rates, owing to the relatively poor fitting of the expression.

The rate constants are virtually identical within experimental error, as are the values for the half-life, $t_{0.5}$. At low extent of reaction, n lies between 1.76 and 2.84. This is consistent with

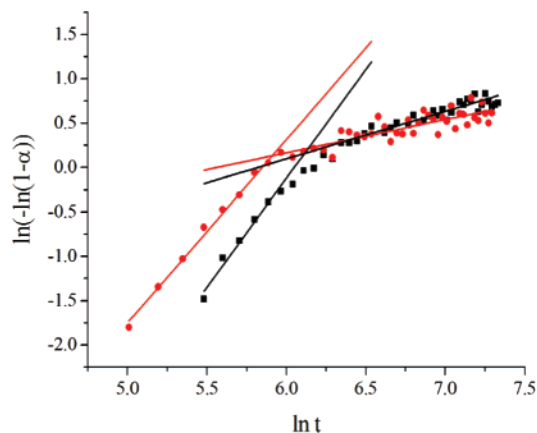


Figure 11. Sharp-Hancock plots for the intercalation of Li_2SO_4 into gibbsite at 70 (black squares) and 90 °C (red circles).

a mechanism which is 2D phase-boundary controlled following deceleratory nucleation. Phase boundary control means that the reaction rate is limited by the rate at which the interlayer space expands to accommodate the guest. If diffusion control operates after the nucleation event, as soon as a pair of layers have been prised apart to accommodate the new guest, the guests diffuse between the layers rapidly. In a phase-boundary controlled system, once the first guest has propped the layers apart, the guests cannot simply diffuse into the interlayer space; to penetrate further into the host lattice they must force their way in. A value of 0.5 for α suggests an entirely diffusion-controlled reaction mechanism, where nucleation plays no part in determining the rate. Therefore, it appears that once the reaction is 60–65% complete, the mechanism changes from 2D phase-boundary controlled following deceleratory nucleation to complete diffusion control.

Although the factors governing this cannot be unequivocally determined, it is believed that the intercalation of Li_2SO_4 into the host introduces significant strain to the crystallites, owing to the large expansion in the interlayer space required to accommodate the guests (the basal spacing seen in situ is $\sim 1/3$ greater for $\text{h-LiAl}_2\text{-SO}_4$ than the other LDHs). This results in the formation of defect sites (represented schematically in Figure 12). These are highly reactive and will react as soon as there is a collision between the defect site and the guest ions. Hence as the reaction proceeds, the increasing number of defect sites available for reaction leads to the adoption of a diffusion-controlled reaction mechanism.

$T \geq 120$ °C. Performing the intercalation of 3 M Li_2SO_4 into gibbsite at 120 °C led to the observation of a curious phenomenon. At $T < 120$ °C, the reaction proceeds from the gibbsite host to the $\text{h-LiAl}_2\text{-SO}_4$ product with a d spacing of 10.3 Å. This is higher than the value observed ex situ owing to the LDH having a higher interlayer water content when suspended in water. However, at 120 °C and higher tempera-

tures, the reaction proceeds via an intermediate phase. This can be seen in the data in Figure 13.

The final product observed has $c = 17.4$ Å ($d_{002} = 8.7$ Å), and the intermediate has a c -parameter of 20.6 Å ($d_{002} = 10.3$ Å). This latter intermediate phase is clearly the same as the final product of the reactions performed below 120 °C. Isolation and drying of the products from all the reactions resulted in phases with $c = 17.4$ Å. Therefore, it seems that the reaction occurring below 120 °C produces a more hydrated form of the phase seen at 120 °C. The phase with $c = 20.6$ Å will henceforth be denoted as the α phase, and that with $c = 17.4$ Å, as the β phase. The same two-stage reaction mechanism is observed when performing the reaction at 130 °C. In contrast to the growth of the α phase at $T < 120$ °C, where a mechanistic change is observed, the Avrami expression may be accurately fitted to the data for the growth of the β phase (with use of an appropriate induction time). Owing to the rapid nature of the growth and decline of the α phase at 120 °C and higher, it is not possible to precisely describe this process with the Avrami model. For the growth of the β phase, the exponent n is approximately 1. This suggests a mechanism which is 2D diffusion controlled following instantaneous nucleation. Unlike the formation of the α phase, the rate of which is largely temperature independent, the rate constant varies significantly with temperature. The activation energy for this process is calculated to be approximately 110 kJ mol $^{-1}$. This high value is likely to be the reason that conversion of the α to the β phase does not occur in situ at lower temperatures. However, when the reaction matrix is filtered and washed, the conversion is facilitated. It seems likely that a high concentration of Li_2SO_4 in solution encourages extrusion of water from the interlayer region to help solvate the Li^+ and SO_4^{2-} ions remaining in solution.

A qualitative observation of the interconversion of the two phases was achieved by performing variable-temperature XRD (Figure 14). In these experiments, a paste was made using the β phase and water. This was then slowly heated, and the temperature evolution of the XRD pattern was monitored. At 59 °C and below, the sole phase present is the more hydrated α phase. As the temperature increases further, and water begins to be evaporated from the paste, reflections corresponding to the β phase grow into the diffraction patterns. At 76 °C, both the α and β phases are present in almost equal amounts. At 78 °C and above, sufficient water has evaporated that only the β phase remains. Additional in situ experiments were used to confirm that the interconversion is a direct, one-step process.

Concentration Studies. The concentration of lithium sulfate was varied between 1 and 3 M at 100 °C. At high concentrations, the reaction mechanism is observed to change at $\alpha \approx 0.4$ –0.6. However, at low concentrations, a constant reaction mechanism is observed. This is illustrated by the Sharp-Hancock plots in Figure 15. The reaction with 2.5 M lithium

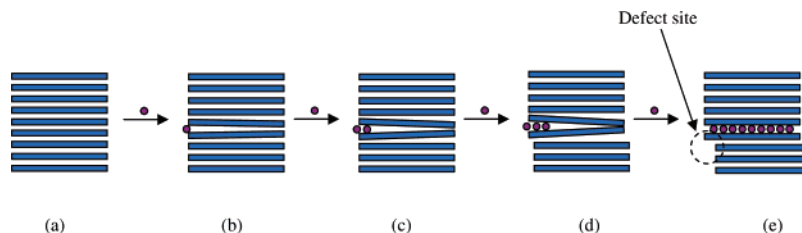


Figure 12. Schematic illustrating how the intercalation of Li_2SO_4 into gibbsite might cause the introduction of defects into the particulates. The layers of the host are shown in blue, and the guest ions are represented as purple circles. In (a) the pristine host prior to reaction is depicted. In (b) and (c) the increase in strain in the particulate as more of the guest ions are intercalated is shown, in (d) the high degree of strain is causing the particle to begin to deform, and in (e) a defect introduced by the strain is illustrated.

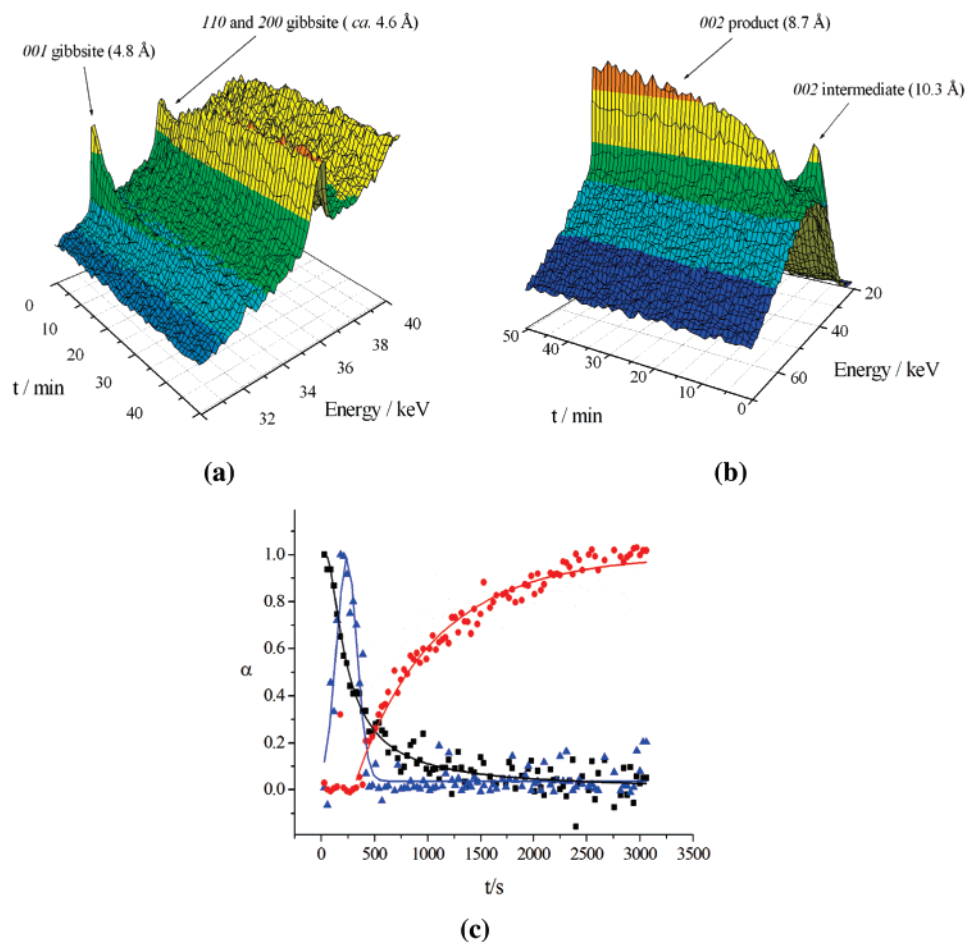


Figure 13. In situ data showing the two-step conversion of gibbsite into $\text{h-LiAl}_2\text{-SO}_4$ at 120 °C: (a) 3D stacked plot showing the decay of the gibbsite reflections with time; (b) 3D plot showing the growth and decline of an intermediate phase and growth of the final product phase; (c) extent of reaction vs time plot showing the gibbsite 001 (black squares), intermediate 002 (blue triangles), and product 002 (red circles) reflections.

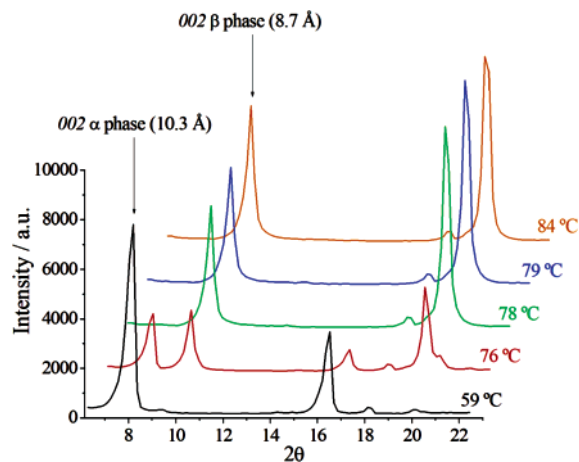


Figure 14. Variable-temperature XRD data for the interconversion of the α and β phases of $\text{h-LiAl}_2\text{-SO}_4$. The reflection at ca. 18° corresponds to the 100 reflection of the LDH in each case.

sulfate shows a change in mechanism with time: in the Sharp–Hancock plot, the gradient of the line changes abruptly at $\ln t \approx 6$. In contrast, the 1 M reaction proceeds via the same mechanism for the entire course of the reaction. From a plot of $\ln k$ vs $\ln [\text{Li}_2\text{SO}_4]$, the order of the reaction with respect to Li_2SO_4 was found to be approximately 1.5. However, owing to the highly complex nature of this process and mechanistic changes, this value should be treated with caution. The mechanistic change that occurs is the same as that discussed earlier. The fact that no mechanistic change occurs when using

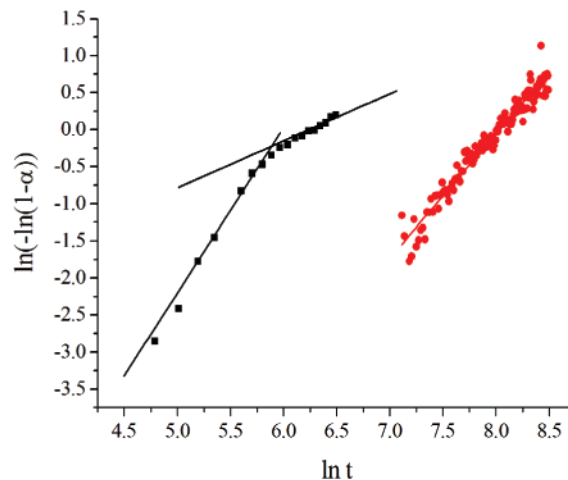


Figure 15. Sharp–Hancock plots for the reaction of gibbsite with 2.5 (black squares) and 1 M (red circles) Li_2SO_4 at 100 °C.

1 M Li_2SO_4 may be tentatively attributed to the fact that the rate of reaction is slow in this case, and hence, the amount of strain induced into the crystallites by reaction is low. This results in the number of defects produced being minimal.

The effect of varying the concentration was also investigated at 120 °C. Using 1 or 1.5 M solutions resulted in processes very closely resembling those occurring at $T < 120$ °C. A direct conversion of gibbsite to the α phase of $\text{h-LiAl}_2\text{-SO}_4$ is observed: none of the β phase is created. Increasing the concentration to 2 M causes both the α and β phases to form.

The α phase is seen to grow in first, and then the β phase grows in following an induction time. In contrast, using a 2.5 M solution of lithium sulfate produces very different looking data. The α phase grows in initially, and the β form begins to grow in later. As the intensity of the 002 reflection corresponding to the β phase increases, it is matched by a decline in the intensity of the α material 002 reflection. The full data are given in the Supporting Information.

Therefore, it can be deduced that the formation of the β phase is influenced by both temperature and the concentration of lithium sulfate. Both high temperatures and high concentrations are needed to convert all of the α phase into the final β product observed *ex situ*.

Intercalation of Li_2SO_4 into Bayerite. The intercalation of lithium sulfate into bayerite was found to be a process very different from the reaction with the gibbsite polymorph. The reaction was very slow, and elevated temperatures (between 130 and 140 °C) were needed to drive the reaction to completion. The reaction was observed to proceed in one step, directly from the host $\text{Al}(\text{OH})_3$ to the $\text{r-LiAl}_2\text{-SO}_4$ product. The product observed *in situ* was analogous to the β phase of the gibbsite intercalate, with a d spacing of 8.6 Å. This is the same as the interlayer spacing seen *ex situ* after drying under vacuum. At all temperatures, n is approximately 1. This suggests that the mechanism is 2D diffusion controlled following instantaneous nucleation. The Arrhenius equation was employed to calculate the activation energy, $E_a = 72.3 \pm 7.9 \text{ kJ mol}^{-1}$, which is consistent with a nucleation governed mechanism.

Intercalation of $\text{Li}(\text{O}_2\text{CCH}_3)$. The intercalation of Li acetate into both gibbsite and bayerite proceeds slowly, and so elevated temperatures (≥ 125 °C) and highly concentrated solutions (10 M) were employed to drive the reaction to completion. At lower temperatures in both cases, n is close to 2. This suggests a mechanism which is 2D phase boundary controlled following instantaneous nucleation, consistent with the large size and low charge of the acetate anions. In the bayerite case, n is reduced from 2 at lower temperatures to 1.5 at higher temperatures. Therefore, it is probable that, at least in the bayerite case, the mechanism is 2D diffusion controlled following deceleratory nucleation. This is also consistent with the gibbsite data where n lies between 1 and 2. The reduction in the value of n for the bayerite reactions reflects the decreasing importance of nucleation at higher temperatures, which is sensible owing to the higher thermal energy of the system and the more rapid transport of guests to the host matrix.

The activation energies are calculated to be 42.0 ± 5.5 and $44.8 \pm 13.6 \text{ kJ mol}^{-1}$ for gibbsite and bayerite respectively, identical within experimental error. These are consistent with processes which are nucleation controlled. The aliphatic tail of the acetate anion will cause slow movement of the ion through the solution owing to the organization of the water molecules around the methyl group. The large interlayer spacing of the final product will mean there is a large energy barrier to the expansion of the interlayer space to accommodate the guests.

Comparison. The above data reveal that the intercalation of Li salts into $\text{Al}(\text{OH})_3$ is a highly complex process, being dependent both on the nature and concentration of the salt and the polymorph of $\text{Al}(\text{OH})_3$ undergoing reaction. Variation of the anion X was found to have a profound effect on the reaction kinetics and mechanisms. The different X anions have different sizes, shapes, and charge distributions. This leads to differing hydration enthalpies, ionic strengths, and extents of dissociation. However, no clear trends may be identified linking these parameters to the phenomena observed experimentally. For

instance, one would expect an anion with a high hydration enthalpy to intercalate slowly, with a correspondingly high activation energy. However, the order of hydration enthalpies is $\text{HO}^- > \text{Cl}^- > \text{NO}_3^-$. The order of activation energy for bayerite is $\text{NO}_3^- > \text{Cl}^- > \text{HO}^-$, and $\text{Cl}^- > \text{HO}^-$ for gibbsite: there seems to be an inverse relationship between hydration enthalpy and activation energy. In contrast, acetate will have a much lower hydration enthalpy than NO_3^- , yet the activation energy order is $\text{NO}_3^- > \text{AcO}^-$. There are significant mechanistic differences between the two $\text{Al}(\text{OH})_3$ polymorphs. No obvious mechanistic trends are observed. However, it is generally the case that the activation energies are somewhat higher for bayerite than for gibbsite. This might be related to the smaller, more irregular, particle sizes of bayerite, and the greater number of nucleation sites. It must be concluded that these are enormously complex processes, with a large number of interlinked factors controlling the reaction kinetics and mechanisms.

Conclusions

The intercalation of five lithium salts into the gibbsite and bayerite polymorphs of $\text{Al}(\text{OH})_3$ has been studied using *in situ* energy dispersive XRD. The kinetics and mechanisms of the reactions have been modeled using the Avrami–Erofe'ev model. The kinetic data suggest that the mechanisms are predominantly nucleation controlled, although the intercalation of LiNO_3 into bayerite and of Li_2SO_4 into gibbsite proceed via two-stage mechanisms, one part of which is diffusion controlled. All the reactions proceed directly from the host to the product except for the intercalation of Li_2SO_4 into gibbsite, where a more hydrated intermediate $\text{h-LiAl}_2\text{-SO}_4$ LDH forms initially, before water is extruded to form the final product. The activation energies calculated from the Arrhenius equation are consistent with the mechanisms proposed, lying in the range 20.9–72.3 kJ mol^{-1} for the intercalation processes.

Acknowledgment. The authors thank Dr. Peter Heines for particle size calculations, Dr. Alex Norquist for helpful discussions, and Dr. Dave Taylor and Mr. Alfie Neild at the Daresbury Laboratory for their assistance. In addition, the EPSRC and St. Hugh's College, Oxford, U.K., are thanked for funding and the CCLRC is thank for access to Station 16.4 at the U.K. SRS.

Supporting Information Available: Reduced time plots for LiCl intercalation into bayerite, extent of reaction vs time and Sharp–Hancock plots for the intercalation of LiCl into bayerite as a function of concentration, *in situ* data showing the reaction of gibbsite with 2 M Li_2SO_4 at 120 °C, *in situ* data showing the reaction of gibbsite with 2.5 M Li_2SO_4 at 120 °C, kinetic parameters for the intercalation of lithium chloride into coarse seed gibbsite, fine seed gibbsite, and activated gibbsite, kinetic parameters for the intercalation of LiOH into gibbsite and bayerite, kinetic parameters for the intercalation of lithium nitrate into bayerite, kinetic parameters for the intercalation of Li_2SO_4 into gibbsite and bayerite, and kinetic parameters for the intercalation of lithium acetate into gibbsite and bayerite. This material is available free of charge via the Internet at <http://pubs.acs.org>.

References and Notes

- (1) Serna, C. J.; White, J. L.; Hem, S. L. *Clays Clay Miner.* **1977**, 25, 384.
- (2) Burba, J. L. I. Crystalline Lithium Aluminates. U.S. Patent 4348295, 1982.
- (3) Nemurdy, A. P.; Isupov, V. P.; Kotsupalo, N. P.; Boldyrev, V. V. *Russ. J. Inorg. Chem.* **1986**, 31, 651.
- (4) Poppelmeier, K. R.; Hwu, S.-J. *Inorg. Chem.* **1987**, 26, 3297.
- (5) Nayak, M.; Kutty, T. R. N.; Jayaraman, V.; Periaswamy, G. J. *Mater. Chem.* **1997**, 7, 2131.

- (6) Besserguenev, A. V.; Fogg, A. M.; Francis, R. J.; Price, S. J.; O'Hare, D.; Isupov, V. P.; Tolochko, B. P. *Chem. Mater.* **1997**, *9*, 241.
- (7) Fogg, A. M.; Freij, A. J.; Parkinson, G. M. *Chem. Mater.* **2002**, *14*, 232.
- (8) Goodenough, R. D.; Stranger, V. U.S. Patent 2980497, 1961.
- (9) Yevteeva, O. G.; Kotsupalo, N. P. *Izv. Sibirsk. Otd. Akad. Nauk SSSR (Ser. Khim. Nauk)* **1968**, *14*, 70.
- (10) Thomas, G. S.; Kamath, P. V. *Mater. Res. Bull.* **2002**, *37*, 705.
- (11) Isupov, V. P.; Kotsupalo, N. P.; Nemurdy, A. P.; Menzheres, L. T. *Stud. Surf. Sci. Catal.* **1999**, *120A*, 621.
- (12) Isupov, V. P.; Chupakhina, L. E.; Belobaba, A.; Trunova, S. J. *Mater. Synth. Process.* **1999**, *7*.
- (13) Isupov, V. P.; Chupakhina, L. E.; Kryukova, G.; Tsybulya, S. *Solid State Ionics* **2001**, *141–142*, 471.
- (14) Isupov, V. P.; Antsiferova, V. A.; Chupakhina, L. E. Russian Federation Patent 1556524, 1988.
- (15) Fogg, A. M.; Green, V. M.; Harvey, H. G.; O'Hare, D. *Adv. Mater.* **1999**, *11*, 1466.
- (16) Lei, L.; Millange, F.; Walton, R. I.; O'Hare, D. *J. Mater. Chem.* **2000**, *10*, 1881.
- (17) Lei, L.; Vijayan, R. P.; O'Hare, D. *J. Mater. Chem.* **2001**, *11*, 3276.
- (18) Fogg, A. M.; O'Hare, D. *Chem. Mater.* **1999**, *11*, 1771.
- (19) Tarasov, K. A.; Isupov, V. P.; Chupakhina, L. E.; O'Hare, D. *J. Mater. Chem.* **2004**, *14*, 1443.
- (20) Thomas, S.; Sherwood, P. M. A. *Anal. Chem.* **1992**, *64*, 2488.
- (21) Clark, S. M.; Cernik, R. J.; Grant, A.; York, S.; Atkinson, P. A.; Gallagher, A.; Stokes, D. G.; Gregory, S. R.; Harris, N.; Smith, W.; Hancock, M.; Miller, M. C.; Ackroyd, K.; Farrow, R.; Francis, R.; O'Hare, D. *Mater. Sci. Forum* **1996**, 228–231, 213.
- (22) Clark, S. M.; Nield, A.; Rathbone, T.; Flaherty, J.; Tang, C. C.; Evans, J. S. O.; Francis, R. J.; O'Hare, D. *Nucl. Instrum. Methods* **1995**, *97*, 98.
- (23) Williams, G. R.; Norquist, A. J.; O'Hare, D. *Chem. Mater.* **2004**, *16*, 975.
- (24) Clark, S. M. *J. Appl. Crystallogr.* **1995**, *28*, 646.
- (25) Sheridan, A. K.; Anwar, J. *Chem. Mater.* **1996**, *8*, 1042.
- (26) Hancock, J. D.; Sharp, J. H. *J. Am. Ceram. Soc.* **1972**, *55*, 74.
- (27) Price, S. J.; Evans, J. S. O.; Francis, R. J.; O'Hare, D. *Adv. Mater.* **1996**, *8*, 582.
- (28) Wilkinson, A. P.; Speck, J. S.; Cheetham, A. J.; Natarajan, S.; Thomas, J. M. *Chem. Mater.* **1994**, *6*, 750.
- (29) Avrami, M. *J. Phys. Chem.* **1940**, *8*, 212.
- (30) Avrami, M. *J. Phys. Chem.* **1941**, *9*, 177.
- (31) Williams, G. R.; Khan, A. I.; O'Hare, D. *Struct. Bonding* **2006**, *119*, 161.
- (32) Rietveld, H. M. *J. Appl. Crystallogr.* **1969**, *2*, 65.
- (33) Isupov, V. P.; Gabuda, S. P.; Kozlova, S. G.; Chupakhina, L. E. *Zh. Strukt. Khim.* **1998**, *39*, 448.